Nano Research

ISSN 1998-0124 CN 11-5974/O4
https://doi.org/10.1007/s12274-019-2275-1

Research Article

Hybrid dual-channel phototransistor based on 1D t-Se and 2D ReS_2 mixed-dimensional heterostructures

Jingkai Qin[1,2,3], Hang Yan[1,3], Gang Qiu[2], Mengwei Si[2], Peng Miao[4], Yuqin Duan[2], Wenzhu Shao[3], Liang Zhen[1,3], Chengyan Xu[1,3] (✉), and Peide D Ye[2] (✉)

[1] *State Key Laboratory of Advanced Welding and Joining, Harbin Institute of Technology, Harbin 150001, China*
[2] *School of Electrical and Computer Engineering, Purdue University, West Lafayette, IN 47907, USA*
[3] *School of Materials Science and Engineering, Harbin Institute of Technology, Harbin 150001, China*
[4] *School of Chemistry and Chemical Engineering, Harbin Institute of Technology, Harbin 150001, China*

Received: 25 October 2018 / **Revised:** 4 December 2018 / **Accepted:** 20 December 2018

ABSTRACT

The combination of mixed-dimensional semiconducting materials can provide additional freedom to construct integrated nanoscale electronic and optoelectronic devices with diverse functionalities. In this work, we report a high-performance dual-channel phototransistor based on one-dimensional (1D)/two-dimensional (2D) trigonal selenium (t-Se)/ReS_2 heterostructures grown by chemical vapor deposition. The injection and separation efficiency of photogenerated electron–hole pairs can be greatly improved due to the high-quality interfacial contact between t-Se nanobelts and ReS_2 films. Compared with bare ReS_2 film devices, the dual-channel phototransistor based on t-Se/ReS_2 heterostructure exhibits considerable enhancement with the responsivity (R) and detectivity (D^*) up to 98 $A{\cdot}W^{-1}$ and 6×10^{10} Jones at 400 nm illumination with an intensity of 1.7 $mW{\cdot}cm^{-2}$, respectively. Besides, the response time can also be reduced by three times of magnitude to less than 50 ms due to the type-II band alignment at the interface. This study opens up a promising avenue for high-performance photodetectors by constructing mixed-dimensional heterostructures.

KEYWORDS

van der Waals heterostructures, ReS_2, trigonal selenium (t-Se) nanobelt, phototransistor

1 Introduction

The van der Waals (vdW) heterostructures based on combination of two-dimensional (2D) layered materials exhibit unique physical properties such as gate-tunability [1, 2], fast charge separation and strong interlayer coupling effect [3–6]. Besides, a number of nonlayered materials with different dimensionalities can be also integrated with 2D layered materials by vdW forces, thereby creating mixed-dimensional vdW heterostructures [7–10]. For example, quadrate PbS nanoplates could be grown on the edge of monolayer MoS_2 to form a hybrid structure, and the device based on the structure exhibits a high photoresponsivity up to 4.5×10^4 $A{\cdot}W^{-1}$ and fast response time less than 7.8 ms [11]. The photodetector based on CdS/MoS_2 heterostructure shows broader wavelength response and 50-fold improvement in photoresponsivity compared with bare MoS_2 devices [12]. Such 2D+nD (n = 0, 1 and 3) combinations have greatly broaden the applications of 2D layered materials in optoelectronic [6, 13, 14], electrochemical [11, 15, 16] and biochemical fields [17–19].

Trigonal selenium (t-Se), as typical one-dimensional (1D) elemental semiconducting material, has a lot of interesting physical properties such as high photoconductivity [20–22], high piezoelectricity [23], and nonlinear optical responses [24, 25]. It possesses a highly asymmetric crystallographic structure, where Se atoms are covalently bonded into helical chains along [001] crystallographic direction, while neighboring chains are stacked together by vdW force to form a hexagonal structure. Specially, the suitable bandgap of 1.7 eV and low dark current makes t-Se widely applied in the UV-to-visible light detect [26]. Thus, it would be of great interest if t-Se could be combined into layered materials to modulate their optoelectronic properties. However, it is still a challenge for t-Se nanostructures to be integrated with 2D layers due to the large difference of lattice parameters [27, 28]. As a unique member of 2D transition metal dichalcogenides (TMDCs), ReS_2 has proven to be highly sensitive to applied light illumination [29]. In addition, it possesses unique distorted 1T' structure (Fig. S1 in the Electronic Supplementary Material (ESM)), which would introduce abundant Re atoms protruding out of the in-plane direction [30]. These protruding Re atoms could act as binding sites for S atoms absorption and result into the vertical growth of ReS_2 by chemical vapor deposition [30–32]. Thus, we expect that such dangling-bond-abundant surface would make ReS_2 a promising platform for subsequent heterogeneous growth of t-Se nanostructures. Very recently, we demonstrated that t-Se nanoplates could be epitaxially grown on monolayer ReS_2 films to form a vertical heterostructure, which exhibits ultrahigh detectivity of up to 8×10^{12} Jones and fast response time of less than 10 ms [33]. However, the isolated small Se nanoplates cannot form a continuous conduction channel for carrier transport, which greatly limits its further applications.

In this work, we demonstrated that t-Se nanobelts can be successfully grown on continuous few-layer ReS_2 films, thereby creating a novel 1D/2D mixed-dimensional heterostructures for photodetection applications. The t-Se nanobelts grow following a wire-by-wire self-assembly mode due to the low surface diffusion energy of ReS_2.

Address correspondence to Chengyan Xu, cy_xu@hit.edu.cn; Peide D Ye, yep@purdue.edu

Dual-channel field-effect transistors (FETs) were fabricated based on such heterostructure, where both Se nanobelts and ReS_2 could act as transport channel. The mixed-dimensional device exhibits a significant enhancement of photoresponse compared with ReS_2-based devices. In addition, due to the efficient injection and separation of photo-excited electron–hole pairs at interface, the response time of the device is greatly reduced by three orders of magnitude to less than 45 ms for rising time and 15 ms for decay time.

2 Experimental

2.1 Growth of ReS_2 and Se/ReS_2 heterostructures

ReS_2 films was grown on mica substrate by chemical vapor deposition (CVD) method. Al_2O_3 boat containing ReO_3 powders was put in the center of the quartz tube, and freshly cleaved fluorophlogopite mica was placed about 1 cm away along the downstream direction. Sulfur powder was placed in another Al_2O_3 boat located upstream direction. The furnace was heated to 600 °C and maintained for 10 min with 40 sccm of Ar. Two types of ReS_2 films were used as substrates for subsequent growth of t-Se nanobelts: few-layer ReS_2 with thickness of ~ 3.1 nm and monolayer ReS_2 (Fig. S2 in the ESM). Figure S3 in the ESM schematically illustrates the two-step growth process of Se/ReS_2 heterostructures. Mica substrate with as-grown ReS_2 films was loaded into a quartz ampoule with Se powder on the other side. The ampoule was vacuumed until pressure lower than 10^{-3} Torr, and then heated at 300 °C for 30 min.

2.2 Characterization

The products were characterized by optical microscopy (Lecia DM4500P), scanning electron microscope (SEM, Hitachi SU-800), atomic force microscope (AFM, Bruker Dimension ICON-PT) and transmission electron microscope (TEM, FEI Talos F200x, acceleration voltage: 200 kV). Raman spectra were recorded using Raman spectrometer (Horiba HR800) with a 633 nm laser. The system was calibrated using Raman peak of Si at 521 cm^{-1}.

2.3 Device fabrication

After the Se/ReS_2 hybrid films were transferred onto SiO_2/Si substrate, the selected overlapped area was first patterned into squares with length of 15 μm by etching with O_2 plasma combined with photolithography process. Then, Ti/Au electrodes with thicknesses of 30/100 nm were fabricated by standard electron beam lithography (EBL) and high-vacuum e-beam evaporation. The width and length of the transport channel were designed to be 10 and 3 μm, respectively. Both the ReS_2 films and Se nanobelts could be contacted with electrodes to form a dual-channel structure.

2.4 Electrical and optoelectrical measurements

Electrical and optoelectrical measurements of the fabricated devices were implemented in a semiconductor instrument (Keithley 4200 SCS) accompanied with a Lakeshore probe station under room temperature and atmospheric pressure. Laser source with different wavelengths calibrated by UV-enhanced silicon photodiode was taken to provide power-tunable illumination. The illumination power to phototransistors was calibrated using power meter (Thorlabs PM100A).

3 Results and discussion

The Se/ReS_2 heterostructure was first characterized by optical microscopy, as shown in Fig. 1(a). Obviously, t-Se nanobelts with gold color could be distinguished from the distinct difference in contrast. According to the AFM topography image (Fig. 1(b)), spindle-like t-Se nanobelts with diameter up to 2 μm are assembled

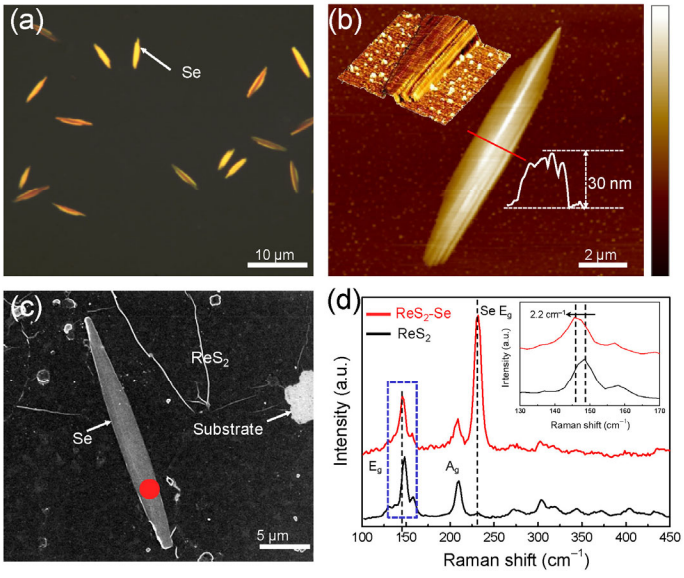

Figure 1 Characterization of Se/ReS_2 mixed-dimensional heterostructures. (a) Optical microscope image of spindle-like t-Se nanobelts on ReS_2 films. (b) AFM height profile of t-Se nanobelts. Inset shows the enlarged three-dimensional (3D) view. (c) SEM image of Se/ReS_2 heterostructure. (d) Comparison of Raman spectra obtained from Se/ReS_2 heterostructure, where the red line is collected from Se/ReS_2 hybrid area (red circle in (c)), and blue line from the bare ReS_2 film.

by parallel narrow nanowires, and they have average height of ~ 30 nm around the center with the length of up to 10 μm. Se nanobelts showing similar morphology could also be grown on monolayer ReS_2 films (Fig. S4 in the ESM). However, these t-Se nanobelts have smaller lateral size (average width < 500 nm) and larger thickness (> 100 nm) compared with that grown on few-layer ReS_2. It is expected to arise from the higher atomic diffusion energy of monolayer ReS_2 surface without defects, which will be discussed later. In the vapor deposition process, the substrate temperature plays an important role in the morphology of the products, which is decided by the location of the substrate in the quartz ampoule [34–36]. In this work, the optimum growth temperature was determined to be 180 °C for growing t-Se nanobelts. Higher deposition temperature would result into the thick t-Se bulks, while lower one gave less dense and small t-Se nanobelts as shown in Fig. S5 in the ESM.

Figure 1(d) displays the Raman spectra of Se/ReS_2 heterostructure and ReS_2 with 633 nm laser excitation at room temperature. Two dominant peaks of ReS_2 located at 150 and 213 cm^{-1} could be assigned to in-plane E_g and out-of-plane A_g vibration modes, respectively. Remarkably, the active Raman E_g mode of t-Se located at 233 cm^{-1}, could also be clearly identified in the Raman spectrum collected from the Se/ReS_2 hybrid area (marked with the red spot in Fig. 1(c)) [21]. It should be mentioned that the E_g mode of ReS_2 in the Se/ReS_2 hybrid films exhibits distinct shift of 2.2 cm^{-1} towards low frequency (inset in Fig. 1(d)). Compared with ReS_2, the conductance level of p-type t-Se located at a higher position, and the efficient electron (hole) transfer between them would lead to the reduction of carrier density in ReS_2, resulting into the weaken of electron–phonon coupling effect and Raman shift in ReS_2 after t-Se growth [36–39].

Hybrid Se/ReS_2 films is transferred onto Cu grid for TEM characterization. The t-Se nanobelt exhibits darker contrast compared with ReS_2 membrane, showing a typical spindle-like structure around the ending area (Fig. 2(a)). High-resolution TEM (HRTEM) image was obtained at the edge of Se/ReS_2 heterostructure marked with red rectangular in Fig. 2(a), where distinct lattice fringes belonging to t-Se can be clearly identified. By combining fast Fourier transform (FFT) pattern with HRTEM (Fig. 2(c)), we can conclude that the single-crystalline t-Se nanobelts are grown along the [001] crystallographic direction. Indeed, the few-layer ReS_2 films are

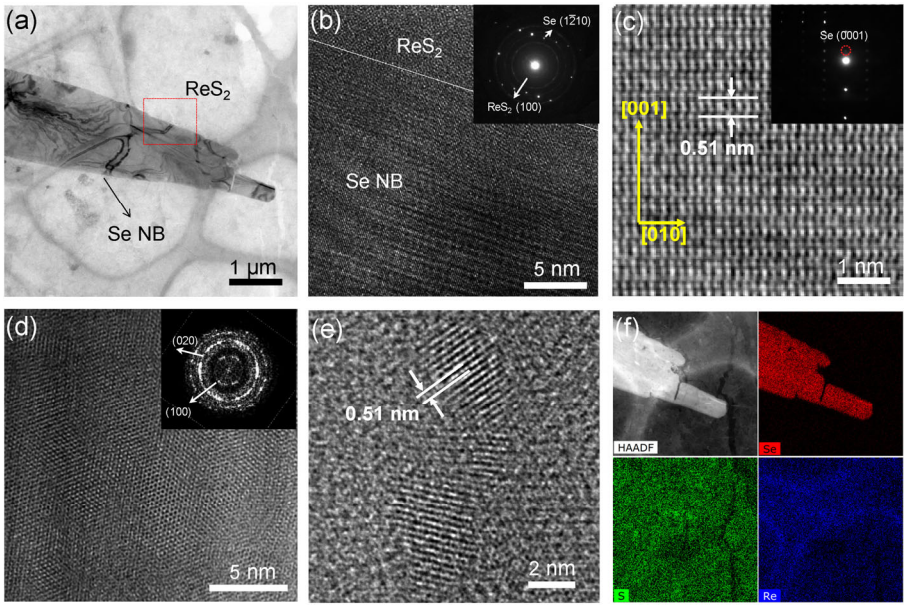

Figure 2 TEM characterization of Se/ReS_2 heterostructures. (a) Bright-field TEM image of Se/ReS_2 heterostructures. (b) HRTEM image of the Se/ReS_2 heterostructures at the edge area (marked with red rectangle in (a)). (c) HAADF-STEM image of t-Se nanobelts. Inset image shows the SAED pattern. (d) HRTEM image of few-layerReS_2 films. Inset image shows the corresponding FET pattern. (e) HRTEM image of t-Se NCs in the initial stage of growth process. (f) EDS elemental mapping of the heterostructure at the ending area.

polycrystal stacked with random-orientated small flakes, which can be demonstrated by the dim diffraction ring as the FFT pattern shows (Fig. 2(d)). It should be noted that highly single-crystallized zero-dimensional (0D) t-Se nanocrystals (NCs) with average diameter of 2 nm were also observed in HRTEM image (Fig. 2(e)). The lattice spacing is estimated to be 0.51 nm, which can be assigned to (001) planes of t-Se. These 0D t-Se nanocrystals are expected to be the products at the initial stage during growth process. Chemical compositions of such hybrid structure are also confirmed by energy dispersive spectrometer (EDS) as shown in Fig. 2(f).

Great interfacial contact of heterojunction would facilitate the energy transfer process between different materials, which would help us to modulate its physical properties more effectively [8, 36, 40]. In this work, AFM scratching method was introduced to evaluate the contact quality of Se nanobelt and ReS_2 films as illustrated in Fig. S6 in the ESM. Remarkably, after t-Se nanobelt being scratched away, the underlying ReS_2 films could be totally lifted off, exposing bare mica substrate. The depth around the pit is about 3.2 nm, which is well in accordance with the thickness of few-layer ReS_2 films, and the corresponding phase image exhibits distinct contrast difference in the exposing area (Figs. S6(c) and S6(d) in the ESM). Besides, Re and S elements can be clearly detected from the EDS mapping image collected from scratched t-Se nanobelts (Fig. S7 in the ESM), indicating that the ReS_2 films are tightly attached on the bottom of t-Se nanobelts. These results strongly demonstrated that the above t-Se nanobelts could contact tightly with underlying ReS_2 films, forming good heterointerface connection. The scratching technique was also applied on t-Se nanobelts grown on monolayer ReS_2 films. Similarly, the underneath ReS_2 is totally lifted off after AFM scratching (Fig. S8 in the ESM).

The ideal interface contact between ReS_2 and Se could be attributed to abundant intrinsic binding sites on ReS_2 surface. As we mentioned before, ReS_2 is a distinct 2D layered material with distorted 1T' structure, and the ultra-low symmetry would introduce lots of protruding Re atoms out of the ReS_2 (001) planes [30]. These unbounded Re atoms with high chemical activity would act seeds for subsequent Se growth, resulting into the covalent bonding of Re and Se atoms at the interface. Besides, these intrinsic protruding Re atoms could also lower the energy barrier for atomic nucleation and migration and facilitate the in-plane growth of t-Se nanobelts. A possible growth mechanism was proposed to explain such nucleation mode as shown in Fig. 3. Due to the highly anisotropic crystal structure of t-Se, and it tends to grow along [001] direction into 1D nanowire [27]. At the first stage, Se atoms would be absorbed on ReS_2 surface and chemically bonded to the protruding Re atoms, resulting into the small clusters (Fig. 3(e)). Due to the low atomic migration energy barrier, these small t-Se clusters adjacent to the ReS_2 surface are likely expanded laterally along in-plane direction into thin nanobelts, while the vertical growth can be partly inhibited due to the higher migration barrier introduced by vdW interaction between Se helical chains [41, 42]. It is worth noting that few-layer ReS_2 films could provide much more active sites compared with

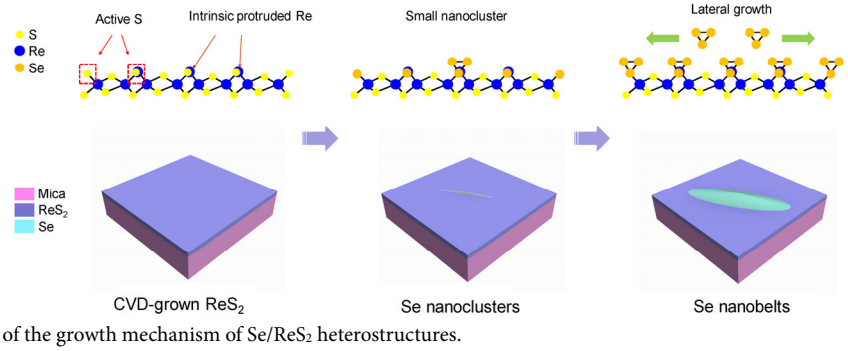

Figure 3 Schematic illustration of the growth mechanism of Se/ReS_2 heterostructures.

monolayer ReS_2 due to the smaller grain size and larger edge-to-area ratio, resulting in the formation of t-Se nanobelts with relatively small thickness and large width.

FETs based on Se/ReS_2 heterostructure were fabricated using Ti/Au as contact on SiO_2/Si substrate. Figure 4(a) shows the optical microscopy image of the device. Both of the ReS_2 films and t-Se nanobelt could contact with device electrodes, thus forming a back-gate transistor with dual conductive channels. The thickness of t-Se nanobelt and few-layer ReS_2 films are about 41 and 3.1 nm, respectively. FETs based on ReS_2 films were also fabricated for comparison. As shown in Fig. S9 in the ESM, the transistor based on ReS_2 films shows distinct n-type transport behavior with high on/off ratio of 10^5, while the hybrid Se/ReS_2 device exhibits a degenerate n-type transport characteristic (Figs. 4(b) and 4(c)). The off-state current in Se/ReS_2 hybrid transistor is increased by three orders of magnitude as negative gate voltage (V_g) is applied, suggesting the transport behavior is dominated by the hole carriers of p-type t-Se nanobelts. On the contrary, the hybrid device exhibits a small on-state current of 3 nA at V_g = 80 V with source-drain voltage (V_{ds}) of 5 V, which is only one-tenth of that in bare ReS_2 devices, indicating that the vertical stacked t-Se nanobelt has a distinct p-doping effect on the underlying ReS_2 films. The carrier mobility could be extracted from the transfer curve using the expression $\mu = L/W\times(1/C_g)\times dG/dV_g$, and it is estimated to be 0.19 $cm^2\cdot V^{-1}\cdot s^{-1}$ for the hybrid transistor. This value is much smaller than that of bare ReS_2 devices (about 3.42 $cm^2\cdot V^{-1}\cdot s^{-1}$ at 300 K). The electron (hole) would transfer between ReS_2 and t-Se nanobelt due to the difference of Fermi level [39, 43], which would cause the reduction of carrier concentration and lead to a depletion region at interface. Thus, the on-state current could be considerable reduced under dark condition. The small on-state dark current could greatly decrease the measuring noise and improve the detectivity of phototransistors [44].

The conduction level (valence level) of trigonal Se and ReS_2 are estimated to be −3.20 eV (−4.92 eV) and −4.25 eV (−6.05 eV), respectively. This difference would lead to the formation of type-II band structure, resulting into the efficient separation of photo-generated electron–hole pairs in Se/ReS_2 heterostructures [39, 43]. The optoelectronic property of Se/ReS_2 mixed-dimensional hetero-structure was also investigated using the same devices. Figure 5(a) presents the schematic structure of the hybrid Se/ReS_2 phototransistor, where the above t-Se nanobelts could act as light absorber to enhance the photoresponse of the devices. As shown in Fig. 5(b), by combining the t-Se nanobelts with ReS_2, the photocurrent in Se/ReS_2 device was enhanced by more than 5 times under zero bias voltage as exposed to 400 nm laser illumination. The source-drain current is greatly increased in the whole range of V_g, and it gradually rises up with the increase of power intensity from 1.7 to 7.4 $mW\cdot cm^{-2}$ (Fig. 5(c)). Figure 5(d) shows the on/off ratio of the phototransistor under dark and light condition at different bias voltages. Compared with the ReS_2 device, the on/off ratio of Se/ReS_2 device is improved by an order of magnitude and it could remain at 200 as V_g scanning from negative to positive, suggesting good stability of Se/ReS_2 device under gate voltage. The photoresponsivity (R) and photodetectivity (D^*) are two important parameters to evaluate the performance of photodetectors. R could be calculated according to the equation $R = I_{ph}/P_{light}$, where I_{ph} is the generated photocurrent and P_{light} represents the incident power intensity. D^* could be obtained using following equation: $D^* = (RA^{1/2})/(2eI_d)^{1/2}$ where A is the effective area of the detector, e is the value of electron charge, and I_d represents the dark current. The photoresponsivity of Se/ReS_2 hybrid phototransistor is estimated to be 98 $A\cdot W^{-1}$ at V_g = 60 V, which is one order higher than that of ReS_2 device (R = 8.7 $A\cdot W^{-1}$). Besides, the D^* of Se/ReS_2 device is calculated

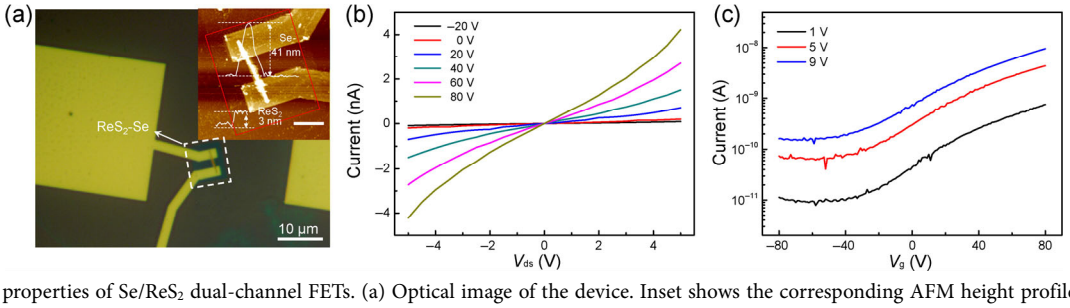

Figure 4 Electrical properties of Se/ReS_2 dual-channel FETs. (a) Optical image of the device. Inset shows the corresponding AFM height profile, and ReS_2 films are marked with red dashed line. Scale bar is 5 μm. (b) Output curves and (c) transfer curves of the device based on Se/ReS_2 heterostructures.

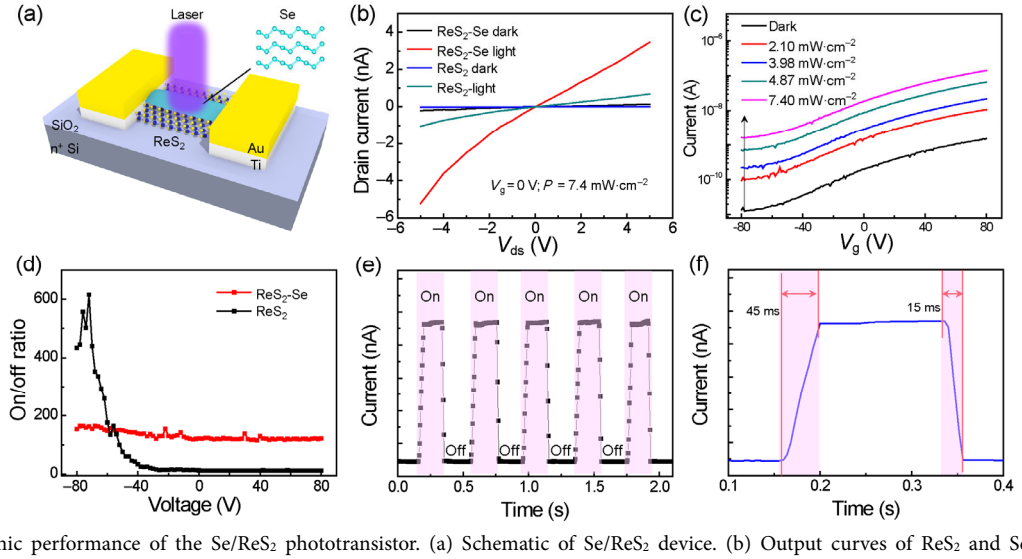

Figure 5 Optoelectronic performance of the Se/ReS_2 phototransistor. (a) Schematic of Se/ReS_2 device. (b) Output curves of ReS_2 and Se/ReS_2 phototransistors. (c) Transfer curves of the device under 400 nm irradiation with different power densities. (d) Bias dependence of the on/off ratios on the two samples. (e)Time-dependent photocurrent measured under chopped light illumination in the hybrid device. (f) A separated response and reset cycle of hybrid devices.

to be 6 × 10^{10} Jones under the same measuring condition, which is comparable with previous reported MoS_2-PbS and WS_2-Bi_2Te_3 hybrid films [40, 45].

The response speed is another critical parameter for photodetectors. Remarkably, the photoresponse time of Se/ReS_2 hybrid device can be significantly reduced as demonstrated by the time–dependent photocurrent (I_{ph}–t) curves in Fig. 5(f). The response and recovery time are estimated to be 45 and 15 ms, respectively, which are almost three orders of magnitude smaller than that of ReS_2 device (15 and 18 s), as shown in Fig. S9 in the ESM. The hybrid device also exhibits an excellent stability without degeneration even after five cycles of alternative illumination (Fig. 5(e)). This excellent response property provides Se/ReS_2 heterostructure a promising application to monitor fast optical signals, and it is also superior than previous reported ReS_2 based phototransistors [13, 32]. Table S1 in the ESM summarizes the important parameters of reported photodetectors based on related mixed-dimensional heterostructures. Obviously, the devices in our work have very high detectivity, great photoresponsivity and relatively fast response.

The enhancement of photoresponse in Se/ReS_2 hybrid device could be well explained by the efficient charge transfer at interface. As mentioned before, both conduction and valence levels of t-Se are located at higher position compared with ReS_2, which would result into a type II band alignment at contact (Fig. 6(b)). As illustrated in Fig. 6(c), the electrons (holes) transfer between t-Se and ReS_2 would cause the depletion of carriers and introduce a built-in field toward ReS_2. Thus, the on-state current could be greatly suppressed under dark condition [7]. Once the light is applied, the photo-generated electrons in t-Se nanobelts can be immediately separated and transferred to ReS_2 driven by the built-in electric field, and photo-excited holes in underlying ReS_2 could also transfer to t-Se nanobelts, which would cause the rising (lowering) of Fermi level in ReS_2 (t-Se nanobelts). The accumulated electrons (holes) in ReS_2 (t-Se nanobelts) could transport through these two channels driven applied electric field of V_{ds} and be captured immediately by the electrodes, resulting in the increase of photocurrent. On the other hand, the modulation of Fermi level would reduce the Schottky barrier at Ti/ReS_2 (Ti/t-Se) interface, which would also facilitate the carrier injection and increase the channel current [8, 10].

As mentioned before, the protruding Re atoms could easily bond with gas molecules from ambient experiment due to the high chemical activity, which would introduce trap states in the band gap and severely deteriorate the response speed [30, 46]. Upon the growth of Se nanobelts, the chemically bonded Se atoms could effectively passivate the surface defects in ReS_2, and the Re–Se bonding at interface can provide a fast transition path for carriers' separation and transfer, leading to the acceleration of response speed. Besides, the potential barrier induced by built-in field at interface would also in turn hinder the carriers transfer back as the light tuned off [9]. Thus, the photo-exited electrons (holes) in ReS_2 (t-Se) could be rapidly recombined, leading to the reduction of recovery time.

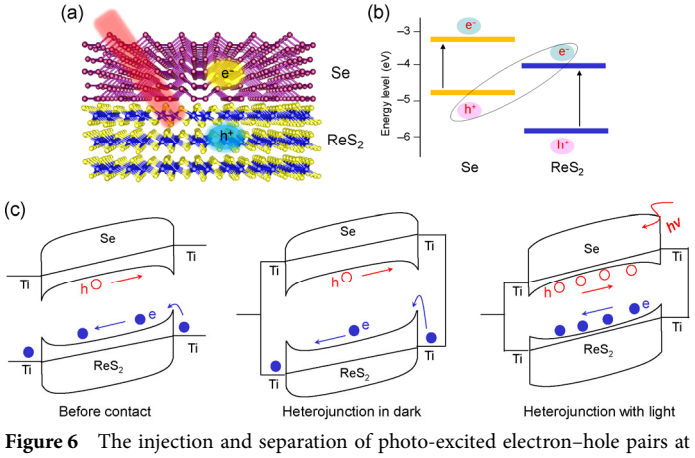

Figure 6 The injection and separation of photo-excited electron–hole pairs at Se/ReS_2 interface. (a) Schematic description for the carrier separation and transport in Se/ReS_2 hybrid structure under light illumination. (b) Band structures of the Se/ReS_2 heterostructure. (c) Schematic diagram of the energy band and carrier transport in Se/ReS_2 heterostructure under dark and light condition.

4 Conclusions

In summary, we reported a vapor disposition approach to obtain Se/ReS_2 mixed-dimensional heterostructures. Due to low surface diffusion energy, t-Se nanobelts could be easily assembled wire by wire, thereby creating a fascinating 1D–2D heterostructure. The high-quality interface contact between t-Se nanobelts and underlying ReS_2 films could efficiently facilitate the charge transfer and separation at interface. The dual-channel phototransistor based on Se/ReS_2 heterostructure exhibits a considerable enhancement in photoresponsivity and photodetectivity compared with the values obtained from bare ReS_2 device under identical illumination. The response time could be considerably reduced by 3 orders of magnitude to less than 50 ms. These findings open up new opportunities to improve the optoelectronic performance of photodetectors by fabricating mixed-dimensional heterostructures.

Acknowledgements

The work is in part supported by the National Natural Science Foundation of China (Nos. 51572057 and 51772064), AFOSR/NSF EFRI 2DARE program, ARO and SRC.

Electronic Supplementary Material: Supplementary material (experimental section and supporting figures) is available in the online version of this article at https://doi.org/10.1007/s12274-019-2275-1.

References

[1] Das, S.; Robinson, J. A.; Dubey, M.; Terrones, H.; Terrones, M. Beyond graphene: Progress in novel two-dimensional materials and van der Waals solids. *Annu. Rev. Mater. Res.* **2015**, *45*, 1–27.

[2] Jariwala, D.; Marks, T. J.; Hersam, M. C. Mixed-dimensional van der Waals heterostructures. *Nat. Mater.* **2017**, *16*, 170–181.

[3] Gao, S. Y.; Yang, L.; Spataru, C. D. Interlayer coupling and gate-tunable excitons in transition metal dichalcogenide heterostructures. *Nano Lett.* **2017**, *17*, 7809–7813.

[4] Jin, C. H.; Kim, J.; Suh, J.; Shi, Z. W.; Chen, B.; Fan, X.; Kam, M.; Watanabe, K.; Taniguchi, T.; Tongay, S. et al. Interlayer electron–phonon coupling in WSe_2/hBN heterostructures. *Nat. Phys.* **2017**, *13*, 127–131.

[5] Li, Y.; Qin, J. K.; Xu, C. Y.; Cao, J.; Sun, Z. Y.; Ma, L. P.; Hu, P. A.; Ren, W. C.; Zhen, L. Electric field tunable interlayer relaxation process and interlayer coupling in WSe_2/graphene heterostructures. *Adv. Funct. Mater.* **2016**, *26*, 4319–4328.

[6] Li, Y.; Xu, C. Y.; Qin, J. K.; Feng, W.; Wang, J. Y.; Zhang, S. Q.; Ma, L. P.; Cao, J.; Hu, P. A.; Ren, W. C. et al. Tuning the excitonic states in MoS_2/graphene van der Waals heterostructures via electrochemical gating. *Adv. Funct. Mater.* **2016**, *26*, 293–302.

[7] Kufer, D.; Konstantatos, G. Photo-FETs: Phototransistors enabled by 2D and 0D nanomaterials. *ACS Photonics* **2016**, *3*, 2197–2210.

[8] Ma, C.; Shi, Y. M.; Hu, W. J.; Chiu, M. H.; Liu, Z. X.; Bera, A.; Li, F.; Wang, H.; Li, L. J.; Wu, T. Heterostructured WS_2/$CH_3NH_3PbI_3$ photoconductors with suppressed dark current and enhanced photodetectivity. *Adv. Mater.* **2016**, *28*, 3683–3689.

[9] Ra, H.-S.; Kwak, D.-H.; Lee, J.-S. A hybrid MoS_2 nanosheet–CdSe nanocrystal phototransistor with a fast photoresponse. *Nanoscale* **2016**, *8*, 17223–17230.

[10] Schornbaum, J.; Winter, B.; Schießl, S. P.; Gannott, F.; Katsukis, G.; Guldi, D. M.; Spiecker, E.; Zaumseil, J. Epitaxial growth of PbSe quantum dots on MoS_2 nanosheets and their near-infrared photoresponse. *Adv. Funct.*

Mater. **2014**, *24*, 5798–5806.
[11] Wen, Y.; Yin, L.; He, P.; Wang, Z. X.; Zhang, X. K.; Wang, Q. S.; Shifa, T. A.; Xu, K.; Wang, F. M.; Zhan, X. Y. et al. Integrated high-performance infrared phototransistor arrays composed of nonlayered PbS–MoS_2 heterostructures with edge contacts. *Nano Lett.* **2016**, *16*, 6437–6444.
[12] Zheng, W.; Feng, W.; Zhang, X.; Chen, X. S.; Liu, G. B.; Qiu, Y. F.; Hasan, T.; Tan, P. H.; Hu, P. A. Anisotropic growth of nonlayered CdS on MoS_2 monolayer for functional vertical heterostructures. *Adv. Funct. Mater.* **2016**, *26*, 2648–2654.
[13] Qin, J.-K.; Ren, D.-D.; Shao, W.-Z.; Li, Y.; Miao, P.; Sun, Z.-Y.; Hu, P. A.; Zhen, L.; Xu, C.-Y. Photoresponse enhancement in monolayer ReS_2 phototransistor decorated with CdSe–CdS–ZnS quantum dots. *ACS Appl. Mater. Interfaces* **2017**, *9*, 39456–39463.
[14] Li, Z. W.; Ye, R. Q.; Feng, R.; Kang, Y. M.; Zhu, X.; Tour, J. M.; Fang, Z. Y. Graphene quantum dots doping of MoS_2 monolayers. *Adv. Mater.* **2015**, *27*, 5235–5240.
[15] Oakes, L.; Carter, R.; Hanken, T.; Cohn, A. P.; Share, K.; Schmidt, B.; Pint, C. L. Interface strain in vertically stacked two-dimensional heterostructured carbon-MoS_2 nanosheets controls electrochemical reactivity. *Nat. Commun.* **2016**, *7*, 11796.
[16] Ansari, S. A.; Cho, M. H. Simple and large scale construction of MoS_2-gC_3N_4 heterostructures using mechanochemistry for high performance electrochemical supercapacitor and visible light photocatalytic applications. *Sci. Rep.* **2017**, *7*, 43055.
[17] Wu, L. M.; Guo, J.; Wang, Q. K.; Lu, S. B.; Dai, X. Y.; Xiang, Y. J.; Fan, D. Y. Sensitivity enhancement by using few-layer black phosphorus-graphene/TMDCs heterostructure in surface plasmon resonance biochemical sensor. *Sens. Actuators B: Chem.* **2017**, *249*, 542–548.
[18] Li, M. Y.; Chen, C.-H.; Shi, Y. M.; Li, L.-J. Heterostructures based on two-dimensional layered materials and their potential applications. *Mate. Today* **2016**, *19*, 322–335.
[19] Pecora, E. F.; Sun, H. D.; Dal Negro, L.; Moustakas, T. D. Deep-UV optical gain in AlGaN-based graded-index separate confinement heterostructure. *Opt. Mater. Express* **2015**, *5*, 809–817.
[20] Kasap, S.; Frey, J. B.; Belev, G.; Tousignant, O.; Mani, H.; Laperriere, L.; Reznik, A.; Rowlands, J. A. Amorphous selenium and its alloys from early xeroradiography to high resolution X-ray image detectors and ultrasensitive imaging tubes. *Phys. Status Solidi B* **2009**, *246*, 1794–1805.
[21] Qin, J. K.; Qiu, G.; Jian, J.; Zhou, H.; Yang, L. M.; Charnas, A.; Zemlyanov, D. Y.; Xu, C.-Y.; Xu, X. F.; Wu, W. Z. et al. Controlled growth of a large-size 2D selenium nanosheet and its electronic and optoelectronic applications. *ACS Nano* **2017**, *11*, 10222–10229.
[22] Wang, K.; Chen, F.; Belev, G.; Kasap, S.; Karim, K. S. Lateral metal-semiconductor-metal photodetectors based on amorphous selenium. *Appl. Phys. Lett.* **2009**, *95*, 013505.
[23] Mukherjee, P.; Konar, S.; Gupta, B. C. Structural and electrical properties of selenium nanotubes. *Phys. Lett. A* **2016**, *380*, 238–241.
[24] Sridharan, K.; Ollakkan, M. S.; Philip, R.; Park, T. J. Non-hydrothermal synthesis and optical limiting properties of one-dimensional Se/C, Te/C and Se–Te/C core–shell nanostructures. *Carbon* **2013**, *63*, 263–273.
[25] Wang, R. P.; Su, X. Q.; Bulla, D.; Wang, T.; Gai, X.; Yang, Z. Y.; Madden, S.; Luther-Davies, B. Identifying the best chalcogenide glass compositions for the application in mid-infrared waveguides. In *Proceedings Volume 9444, International Seminar on Photonics, Optics, and Its Applications*, Bali, Indonesia, 2015.
[26] Yang, W.; Hu, K.; Teng, F.; Weng, J. H.; Zhang, Y.; Fang, X. S. High-performance silicon-compatible large-area UV-to-visible broadband photodetector based on integrated lattice-matched type II Se/n-Si heterojunctions. *Nano Lett.* **2018**, *18*, 4697–4703.
[27] Gao, X. Y.; Gao, T.; Zhang, L. D. Solution–solid growth of α-monoclinic selenium nanowires at room temperature. *J Mater. Chem. Mater.* **2003**, **13**, 6–8.
[28] Luo, L. B.; Jie, J. S.; Chen, Z. H.; Zhang, X. J.; Fan, X.; Yuan, G. D.; He, Z. B.; Zhang, W. F.; Zhang, W. J.; Lee, S. T. Photoconductive properties of selenium nanowire photodetectors. *J. Nanosci. Nanotechnol.* **2009**, *9*, 6292–6298.
[29] Liu, E. F.; Long, M. S.; Zeng, J. W.; Luo, W.; Wang, Y. J.; Pan, Y. M.; Zhou, W.; Wang, B. G.; Hu, W. D.; Ni, Z. H. et al. High responsivity phototransistors based on few-layer ReS_2 for weak signal detection. *Adv. Funct. Mater.* **2016**, *26*, 1938–1944.
[30] Ghoshal, D.; Yoshimura, A.; Gupta, T.; House, A.; Basu, S.; Chen, Y. W.; Wang, T. M.; Yang, Y.; Shou, W. J.; Hachtel, J. A. et al. Theoretical and experimental insight into the mechanism for spontaneous vertical growth of ReS_2 nanosheets. *Adv. Funct. Mater.* **2018**, *28*, 1801286.
[31] Cui, F. F.; Wang, C.; Li, X. B.; Wang, G.; Liu, K. Q.; Yang, Z.; Feng, Q. L.; Liang, X.; Zhang, Z. Y.; Liu, S. Z. et al. Tellurium-assisted epitaxial growth of large-area, highly crystalline ReS_2 atomic layers on mica substrate. *Adv. Mater.* **2016**, *28*, 5019–5024.
[32] Li, X. B.; Cui, F. F.; Feng, Q. L.; Wang, G.; Xu, X. S.; Wu, J. X.; Mao, N. N.; Liang, X.; Zhang, Z. Y.; Zhang, J. et al. Controlled growth of large-area anisotropic ReS_2 atomic layer and its photodetector application. *Nanoscale* **2016**, *8*, 18956–18962.
[33] Qin, J. K.; Qiu, G.; He, W.; Jian, J.; Si, M.-W.; Duan, Y.-Q.; Charnas, A.; Zemlyanov, D. Y.; Wang, H.-Y.; Shao, W.-Z. et al. Epitaxial growth of 1D atomic chain based se nanoplates on monolayer ReS_2 for high-performance photodetectors. *Adv. Funct. Mater.* **2018**, *28*, 1806254.
[34] Li, Y. T.; Huang, L.; Li, B.; Wang, X. T.; Zhou, Z. Q.; Li, J. B.; Wei, Z. M. Co-nucleus 1D/2D heterostructures with Bi_2S_3 nanowire and MoS_2 monolayer: One-step growth and defect-induced formation mechanism. *ACS Nano* **2016**, *10*, 8938–8946.
[35] Miwa, J. A.; Dendzik, M.; Grønborg, S. S.; Bianchi, M.; Lauritsen, J. V.; Hofmann, P.; Ulstrup, S. Van der Waals epitaxy of two-dimensional MoS_2–graphene heterostructures in ultrahigh vacuum. *ACS Nano* **2015**, *9*, 6502–6510.
[36] Zhou, X.; Gan, L.; Tian, W. M.; Zhang, Q.; Jin, S. Y.; Li, H. Q.; Bando, Y.; Golberg, D.; Zhai, T. Y. Ultrathin $SnSe_2$ flakes grown by chemical vapor deposition for high-performance photodetectors. *Adv. Mater.* **2015**, *27*, 8035–8041.
[37] Das, A.; Pisana, S.; Chakraborty, B.; Piscanec, S.; Saha, S. K.; Waghmare, U. V.; Novoselov, K. S.; Krishnamurthy, H. R.; Geim, A. K.; Ferrari, A. C. et al. Monitoring dopants by Raman scattering in an electrochemically top-gated graphene transistor. *Nat. Nanotechnol.* **2008**, *3*, 210–215.
[38] Suh, J.; Park, T. E.; Lin, D. Y.; Fu, D. Y.; Park, J.; Jung, H. J.; Chen, Y. B.; Ko, C.; Jang, C.; Sun, Y. H. et al. Doping against the native propensity of MoS_2: Degenerate hole doping by cation substitution. *Nano Lett.* **2014**, *14*, 6976–6982.
[39] Joshi, S. S.; Lokhande, C. D. Fabrication of isotype (p-p) selenium-polyaniline heterojunction diode by electrochemical method. *Appl. Surf. Sci.* **2006**, *252*, 8539–8543.
[40] Kufer, D.; Nikitskiy, I.; Lasanta, T.; Navickaite, G.; Koppens, F. H. L.; Konstantatos, G. Hybrid 2D–0D MoS_2–PbS quantum dot photodetectors. *Adv. Mater.* **2015**, *27*, 176–180.
[41] Liu, Y. Y.; Wu, W. Z.; Goddard, W. A., III. Tellurium: Fast electrical and atomic transport along the weak interaction direction. *J. Am. Chem. Soc.* **2018**, *140*, 550–553.
[42] Ren, L.; Zhang, H. Z.; Tan, P. H.; Chen, Y. F.; Zhang, Z. S.; Chang, Y. Q.; Xu, J.; Yang, F. H.; Yu, D. P. Hexagonal selenium nanowires synthesized via vapor-phase growth. *J. Phys. Chem. B* **2004**, *108*, 4627–4630.
[43] Liu, H. M.; Xu, B.; Liu, J. M.; Yin, J.; Miao, F.; Duan, C.-G.; Wan, X. G. Highly efficient and ultrastable visible-light photocatalytic water splitting over ReS_2. *Phys. Chem. Chem. Phys.* **2016**, *18*, 14222–14227.
[44] Perini, C. A. R.; Barker, A, J.; Sala, M.; Petrozza, A.; Caironi, M. High speed solution-processed hybrid perovskite photodetectors with low dark current enabled by a low temperature metal oxide interlayer. *Semicond. Sci. Technol.* **2018**, *33*, 094004.
[45] Yao, J. D.; Zheng, Z. Q.; Yang, G. W. Layered-material WS_2/topological insulator Bi_2Te_3 heterostructure photodetector with ultrahigh responsivity in the range from 370 to 1550 nm. *J. Mater. Chem. C* **2016**, *4*, 7831–7840.
[46] Wang, Q. S.; Safdar, M.; Xu, K.; Mirza, M.; Wang, Z. X.; He, J. Van der Waals epitaxy and photoresponse of hexagonal tellurium nanoplates on flexible mica sheets. *ACS Nano* **2014**, *8*, 7497–7505.